JOINT INSTITUTE FOR NUCLEAR RESEARCH
Frank Laboratory of Neutron Physics

FINAL REPORT ON THE
START PROGRAMME

Characterization by nuclear and related techniques of the influence of the method of growth and irradiation on the structural properties of samples of semiconductor materials based on PbS to be used as space solar cells.

Supervisor:
Dr. Aleksandr Sergeyevich Doroshkevich

Student:
BSc. Ronaldo R. Méndez Hernández, Cuba
University of Havana

Participation period:
September 03 – October 28,
Summer Session 2023

-Dubna, 2023-

Abstract

Semiconductors and semiconductor materials are used in the manufacture of microelectronic and optoelectronic devices like transistors, diodes, integrated circuits, photodetectors, and solar cells. These materials can be altered by dopants, an applied electric field, or electromagnetic radiation. Silicon (Si) is the most widely used semiconductor material, but there are other types such as electrical semiconductors and compound semiconductors. In the last decade, chalcogenide semiconductors have been investigated for applications in the field of applied technology due to their efficiency and diverse properties. Lead sulfide (PbS) is a popular direct narrow-band-gap semiconductor, used in infrared technology and optoelectronics for thin-film detectors. PbS films can be deposited using methods like chemical bath deposition, vacuum deposition, electrochemical deposition, and spray pyrolysis. The magnetron ion sputtering growth method is one of the major physical methods for preparing PbS films. In the present research, the concentration profiles of different configurations of PbS-based samples of semiconductor materials were obtained, as well as a characterization of the structural behavior of these samples after being submitted to doses of proton radiation within the range of ($10^{14}\ {}^{part}/_{cm^2} - 10^{17}\ {}^{part}/_{cm^2}$).

Keywords: lead sulfide films, semiconductor materials.

__Content__

-Dubna, 2023-

Introduction

The incredible properties of semiconductors and semiconductor materials make possible its use in the manufacture of microelectronic and optoelectronic devices such as transistors, diodes, integrated circuits, photodetectors, and solar cells. Due to the electrical properties of these materials can be altered by using dopants, an applied electric field, or electromagnetic radiation. According to the number of valence shell electrons in a semiconductor material, these materials are located between insulators (poor electrical conductors) and metals (good semiconductors). As discrete components, they have found use in power devices, optical sensors, and light emitters, including solid-state lasers, all these due to their compactness, reliability, power efficiency, and low cost.

Although silicon (Si) is the most widely used semiconductor material today, other types of semiconductor materials are also available. In this sense, there are two basic categories of semiconductors and semiconductor materials: electrical semiconductors and compound semiconductors. Like Si, germanium (Ge) is other of the most common electrical semiconductors, both being usually used in many semiconductor components. Gallium arsenide (GaAs) and indium phosphide (InP) are examples of composite semiconductors that contain added materials or dopants. Semiconductor doping, the addition of a very small amount of a foreign substance to a pure semiconductor crystal, provides a semiconductor with an excess of conducting electrons or an excess of conducting holes. In addition to the previous materials, lead sulfide (PbS) also represents semiconductor compound that appear within the group of typical small gap semiconductors.

This compound is a representative of the abundant family of semiconducting chalcogenides,[1] being one of the most demanded narrows-bandgap ($0.41\ eV$ at room temperature for coarse-grained samples) semiconductors. Related to the above, it is important to mention that the narrow band gap of this compounds tends to vary depending on the type of structure in which the sample crystallizes. Lead sulfide films (PbS films) are widely used in infrared (IR) technology and optoelectronics for production of thin-film detectors operating in the IR spectral region. Nanostructured lead sulfide, mainly in the form of films, allows to extent the spectral region of IR detectors intended to detect heat sources, allowing us to reach the ultraviolet (UV) region [1]. Furthermore, these films are used in the design of photoelectric multipliers, night-viewing devices, and optical switchers [2]. In addition to the above, these materials focus their field of application in fire sensor systems, flame sensors, and heat source detection systems, so the thermal stability of the nanocrystalline state determines to a significant degree the feasibility of using nanoparticulate PbS in those devices that use them [3]. Recently, solar cells based on a PbS nanocrystalline thin film is also receiving a lot of attention [4]. In addition to the above, it is important to

---

[1] A chalcogenide is a chemical compound consisting of at least one chalcogen anion and at least one more electropositive element. Although all group 16 elements of the periodic table are defined as chalcogens, the term chalcogenide is more commonly reserved for sulfides, selenides, tellurides, and polonides, rather than oxides.

highlight that PbS can be deposited by a variety of methods such as chemical bath deposition (CBD) [5], vacuum deposition [6], electrochemical deposition [7], and spray pyrolysis [8]. Among the physical methods for the preparation of PbS films, the major ones are various alternatives of gas phase deposition [9]. Compared with other preparation of PbS thin films, magnetron sputtering growth technique has the advantage of generating few impurities, as well as precise control of the film structure, thus constituting a potential method to deposit PbS thin films. Precisely this technique was used to obtain and synthesize the samples studied in the present work.

Current research has focused on the effects of high energy radiation on semiconductor solar cells is crucial for space applications. These cells power vehicles in environments with high energy electrons and protons from Earth's radiation belts. It is well known that protons in these radiation belts exhibit energies ranging from the lowest energies measured by spacecraft detectors (a few keV) to energies of tens of BeV. Typical fluxes reported have been about $3 \cdot 10^8 \ protons/cm^2 s$ with energies between 0.5 and 1.0 MeV, and about $10^{15} \ protons/cm^2 s$ with energies between 1 and 80 MeV [20]. Often satellites are expected to function for periods as long as ten years. If a satellite orbit were confined to regions of maximum flux levels, the integrated flux over such a ten-year period would be about $4 \cdot 10^{13} \ protons/cm^2$ with energies between 1 and 80 MeV [10]. In addition, the satellite would have been irradiated by about $10^{17} \ protons/cm^2$ with energies between 0.5 and 1.0 MeV. To be sure it is easy to shield against these low energy protons, but their presence must still be taken into account and above all you must know the main effects that these radiations produce on these devices.

Among the reasons why it is important to study the effects of this type of radiation on these materials, it is worth mentioning:

- Such studies provide experimental data which can be used to test the models devised to explain the behavior of such cells.
- Irradiation by protons of very low energy and, therefore, low range, can help to establish relative contributions to the photovoltaic effect from various regions of the cells.
- The effects of this type of radiation make it possible extraction of fundamental information about the radiation damage process in the semiconductors from which the cells are made.
- This type of study allows us to better understand how the process of annealing of radiation damage occurs which in turn can be related to more fundamental parameters of the material.
- Understanding these radiation effects helps test models and extract fundamental information about radiation damage processes.

Therefore, when some kind of photovoltaic cell is being considered for space applications it is imperative to examine the effects of irradiation on these cells and to compare their performance to that of the silicon cells.

Taking all of the above as justification, it is clear that there is adequate motivation for studying the effects of radiation damage on thin film photovoltaic cells. In this sense,

this project constitutes a summary of the main results obtained from the characterizations of thin films of PbS samples, grown by the Dr. C. Abel Fundora Cruz research group, in collaboration with the Research Center on Physical and Mathematical Sciences at the Autonomous University of Nuevo León, Mexico, to be used for the manufacture of space solar cells.

Proposed Scientific Tasks

Raised all the above, it becomes necessary the study of the influence of the growth methods, and irradiation over the structural properties of PbS thin film samples grown on different substrates for their potential use as space solar cells. In this sense, the proposed tasks to be carried out with this set of samples were:

1. Characterization of PbS samples in their initial state (before being irradiated) using Rutherford Backscattering Spectrometry (RBS) and Particle-Induced X-ray Emission (PIXE) techniques to obtain elemental compositional quantification of these samples.

2. Irradiate these samples with proton beams at different flow regimes (10^{14} $^{protons}/_{cm^2} - 10^{17}$ $^{protons}/_{cm^2}$) for further electrical and structural characterization.

<u>Materials and methods</u>

As part of this chapter, some characteristics of PbS are presented, the growth method used to obtain these samples is discussed, as well as the operating principles of the techniques used for sample characterizations.

Lead sulfide

PbS is a black semiconductor from the IV–VI group with a band gap of 0.4 eV at 300 K [11]. It is an ideal candidate for fabrication of thin film solar cell due to its efficient light absorbing capacity from the visible to near infrared region, relatively long-excitonic-lifetime (200–800ns), high-quantum-efficiency (80%), relatively large excitation Bohr radius (18 nm), water solubility, etc. [12]. Further the band gap of PbS can be tuned from 0.41 eV to 2.3 eV by changing the mean nanocluster size [13].

PbS exhibits both *n*-type and *p*-type conductivity, which narrow band gap tends to vary depending on the type of structure in which the sample crystallizes. In addition, it has a large exciton Bohr radius of $18\,nm$ making it suitable to use in many of the applications previously mentioned in the introduction and has been studied by many researchers in the synthesis of quantum dots for the improvement of solar cells and not so in nanostructured thin films, due to its difficult to obtain by chemical methods [1].

The physicochemical properties of semiconductor nanomaterials differ substantially from the properties of their coarser-grained analogues due, fundamentally, to three key reasons:

- The size of the nanoparticles is comparable to the radius of the excitons in semiconductors, which influences the electronic, optical, and luminescent properties of these compounds.
- The small size of the grains determines a larger surface area of the particles; When the grain size is 100 to 1 nm, the surface houses 1 to 50% of the atoms of the solid, so the surface atoms mostly influence the properties of the nanomaterial.
- The appropriate size of nanoparticles is close to the size of a molecule.

Growth method

Although the synthesis of these samples is not part of the present project, it worth to mention some details in this regard for the correct understanding of many of the experimental results obtained.

The methods used to obtain nanostructured chalcogenide films can be classified into chemical and physical ones. Although there are many methods of growth, chemical bath deposition is the most used method for the preparation of PbS thin films. However, PbS thin films prepared using this method require a long preparation time. For the present study, nanostructured PbS thin films were deposited on glass substrates at room temperature by magnetron sputtering technique using a radio frequency source with power values of 80, 90 or 150 W for the case of simple PbS samples, and power values of 50, 100 or 120 W for PbS/CdS multilayer samples. The eroding gas used was Ar, whose flux was also varied in the simple PbS samples with values of 80, 90 or 100 sccm, while in the case of the three PbS/CdS multilayer samples, it remained constant (60 sccm). Argon flow time were kept constant, being 30 min in both groups for the same. Besides, the base pressure was of the order of 10^{-5} Torr, which was achieved by means of a turbomolecular pump, the working pressures were close to 10^{-3} Torr. Finally, the PbS and PbS/CdS samples were deposited on BK7 and ITO glass respectively.

During the current period, 7 of the PbS samples presented were measured, which information is tabulated below:

No. Identifier	Sample label	Power applied (W)	Ar flux (sccm)	Argon flow time (min)
1	PbS_47	150	80	30
2	PbS_46	150	90	30
3	PbS_41	150	100	30
4	PbS_61	80	90	30
5	PbS_20/CdS_12/ITO	100	60	30

| 6 | PbS_22/CdS_14/ITO | 120 | 60 | 30 |
| 7 | PbS_23/CdS_15/ITO | 50 | 60 | 30 |

Only the following sample remains to be studied from this first group:

No. Identifier	Sample label	Power applied (W)	Ar flux (sccm)	Argon flow time (min)
8	PbS_37	80	100	30

Rutherford Backscattering Spectrometry

Rutherford Backscattering Spectrometry (RBS) is a nuclear method used for near surface layer analysis of solids. It involves bombarding a target with ions at an energy in the MeV-range, typically 0.5-4 MeV, and recording the energy of backscattered projectiles using an energy-sensitive detector, typically a solid-state detector. This technique provides accurate depth information (which accuracies is around a few percent, with 10–30 nm in depth resolution) about the stoichiometry, elemental area density, and impurity distributions of individual elements in the near surface region of bulk materials and in thin films [14]. It is non-destructive, has good depth resolution of several nm, and has a very good sensitivity for heavy elements of the order of parts-per-million (ppm). The results obtained typically do not require the use of standards and are insensitive to the sample chemical bonding, and in addition, it is a quick and easy experiment to perform, typically with data acquisition times of a few tens of minutes. The analyzed depth is typically about 2 μm for incident He-ions and about 20 μm for incident protons.

RBS includes all types of elastic ion scattering with incident ion energies in the range 500 keV – several MeV. Protons, ^{4}He, and sometimes lithium ions are used as projectiles at backscattering angles of 150–170º. Regarding the experimental geometry of this technique, it can be said that the most often used scattering geometries are presented in Fig. 1.
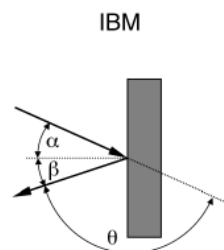
Figure 1: IBM geometry: Incident angle α, exit angle β and scattering angle θ.

In IBM geometry incident beam, exit beam and surface normal of the sample are in the same plane, with:

$$\alpha + \beta + \theta = 180°$$

The experimental setup for a backscattering experiment is shown in Fig.2.
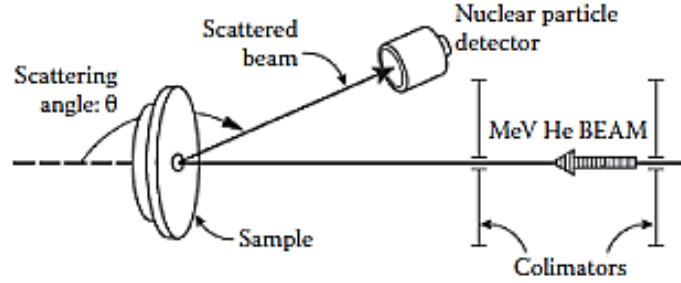
Figure 2: Schematic of the experimental setup of a backscattering experiment.

From a mathematical point of view, the physical foundations of this technique start from considering the energy E_1 of a backscattered projectile with incident energy E_0 and mass M_1 after scattering, whose relationship is given by the expression:

$$E_1 = KE_0$$

where the kinematic factor K is given by

$$K = \frac{M_1^2}{(M_1 + M_2)^2} \left\{ \cos\theta \pm \left[\left(\frac{M_2}{M_1} \right)^2 - \sin^2\theta \right]^{1/2} \right\}^2$$

θ is the scattering angle and M_2 the mass of the target nucleus initially at rest. For $M_1 < M_2$ only the plus sign in the last equation applies.

For the case of two different target elements with mass difference ΔM_2, the energy separation ΔE_1 of particles backscattered from the two masses is given by:

$$\Delta E_1 = E_0 \frac{dK}{dM_2} \Delta M_2.$$

It is important to highlight that, as can be seen from Fig. 3, the best energy separation and mass resolution are obtained for light target elements, while mass resolution gets small for heavy elements. The explanation of the later sentence is due to that for these elements the derivative dK/dM_2 is steep, while for heavy elements the mass resolution gets small.

-Dubna, 2023-
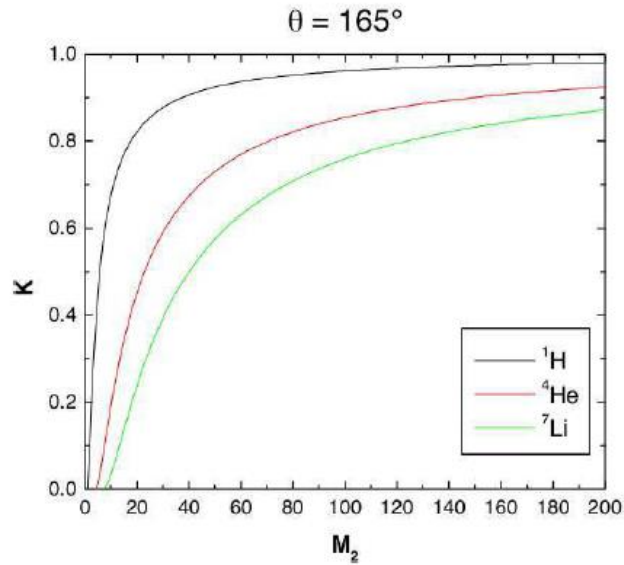
Figure 3: *The kinematic Factor K, as a function of target mass M_2, is shown in Fig. 2 for incident protons, ^{4}He, and ^{7}Li ions at a scattering angle of 165°.*

Several computer codes for the simulation and data evaluation of RBS spectra have been developed over the last two decades, each with its own advantages and disadvantages. Often used codes for the simulation of RBS spectra are RUMP [15], RBX [16], and SIMNRA [17]. These codes are spectrum simulators, i.e. they calculate a spectrum for a given target structure and allow fitting of target compositions to measured spectra.

Particle-Induced X-ray Emission Analysis

Particle-induced x-ray emission (PIXE) is an analytical technique that uses the occasional ejection of inner-shell electrons from target atoms by energetic particle impact and the spectroscopy of the subsequently emitted x-rays during the electronic deexcitations. Such deexcitation occurs when a vacancy is created in one of the inner shells, which must then be filled by an electron from an outer shell. These basic principles of PIXE are schematically illustrated in Fig.4.
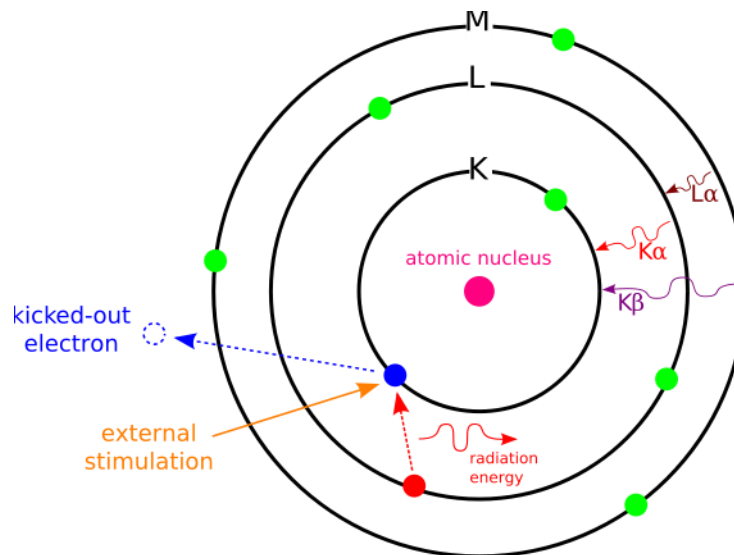
Figure 4: *Schematic picture of the PIXE principle. A charged particle knocks out an electron from one of the inner electron shells (left). The vacancy created is filled by an electron from an outer shell, in which process an X-ray photon is emitted (right).*

The complete PIXE analysis involves two basic aspects: assigning observed x-ray peaks energies to appropriate elements (element identification) and converting observed x-ray peaks (areas) into elemental concentrations (concentration quantification) [18].

Generally, the X-rays generated are registered by using a Si (Li)-detector, producing an X-ray energy spectrum with characteristic peaks corresponding to the elements in the sample. In these spectra, the height of these peaks is proportional to the concentration of the elements. By measuring beam current and understanding the physical processes involved like cross-sections, fluorescence yields, detector efficiency, etc, one can determine the concentration in an absolute way without relying on calibrations and standards [18].

RBS and PIXE Measurement Details

To determine the operating parameters of the accelerator, a standard sample of SiO_2/Si was measured in all cases in at least one (or both) of the direction used for the analysis of the samples of interest. Measurements were made on each sample at two angles of incidence $0°$ and $30°$. In most cases, the behaviour of the detector was quite stable except for the acquisition made for the sample PbS_22/CdS_14/ITO with incident angle of $30°$ with respect to the normal surface whose spectrum label is identified as SV176, for which a percentage detector dead time of 1.8% was recorded. The above value, although somewhat altered, is not a problem since the operational range of validity of the measurement reaches up to 3% or 5% of percentage dead time. Experimentally, the samples were irradiated with an ion beam $^4He^{++}$ of 2 MeV, whose beam spot diameter was around 1 mm.

WinADC software was used for RBS acquisition and Amptek's DPPMCA software was used for PIXE spectrum acquisition. The acquisition was performed in each case for

about 30 to 50 minutes depending on the acquired statistic. It is important to note that both techniques were performed simultaneously since the experimental set-up allows it.

The measurement information for each sample is tabulated below:

Samples	RBS	Filename	PIXE	Filename
PbS_41	20-09-2023	SV 177 60°	20-09-2023	PI 292 60°
		SV 178 90°		PI 293 90°
PbS_22/CdS_14/ITO	20-09-2023	SV 175 90°	20-09-2023	PI 290 90°
		SV 176 60°		PI 291 60°
PbS_46	20-09-2023	SV 182 60°	20-09-2023	PI 296 60°
	21-09-2023	SV 183 90°	21-09-2023	PI 297 90°
PbS_47	21-09-2023	SV 189 60°	21-09-2023	PI 302 60°
		SV 190 90°		PI 303 90°
PbS_20/CdS_12/ITO	21-09-2023	SV 191 90°	21-09-2023	PI 304 90°
	22-09-2023	SV 192 60°	22-09-2023	PI 305 60°
PbS_61	22-09-2023	SV 193 60°	22-09-2023	PI 306 60°
		SV 194 90°		PI 307 90°
PbS_23/CdS_15/ITO	22-09-2023	SV 200 60°	22-09-2023	PI 312 60°
		SV 201 90°		PI 313 90°

RBS spectra obtained by WinADC was processing using SIMNRA software version 7.02, which is a Microsoft Windows software for the simulation of energetic spectra of charged particles and γ-ray yields for the analysis with ion beams whose energy of incident ion varies from approximately 100 keV to many MeV [17].

By SIMNRA simulation, the fitting of the simulated and experimental spectra was carried out, considering, according to the suggestion of the program manual, an acceptable fitting when the X_r^2 parameter is in the range of 3 to 5, and an excellent fit if this statistical parameter is between 1 and 2 [17].

The values of the experimental parameters in which the different measurements were carried out were tabulated and can be found in Annex 1 of this report. The information related to the energy calibration of the RBS spectra as well as its corresponding verification is summarized as part of Annex 3.

It is worth mentioning that in relation to the calibration of the PIXE spectra in the Amptek-dpp software, data set of Si and Ge X-Ray Emission Lines is used, which values is shown below:

Channel	Energy (keV)
688.79	1.74
3848.32	9.88

-Dubna, 2023-

Irradiation details

In recent years, considerable effort has been devoted to investigations of the effects of high energy radiation on space solar cells, since photovoltaic cells are primarily used to power long-operating space vehicles in environments containing high energy electrons and protons from Earth's radiation belts. In these regions of space, typical fluxes reported have been about $3 \cdot 10^8 \ protons/cm^2 s$ with energies between 0.5 and 1.0 MeV, and about $10^{15} \ protons/cm^2 s$ with energies between 1 and 80 MeV. In addition to the above, most satellites are designed to operate for periods as long as ten years. If a satellite orbit were confined to regions of maximum flux levels, the integrated flux over such a ten-year period would be about $4 \cdot 10^{13} \ protons/cm^2$ with energies between 1 and 80 MeV, and about $10^{17} \ protons/cm^2$ within the energetic range between 0.5 and 1.0 MeV [10].

Taking the above into account, two samples with different configurations were selected to study the effect of proton radiation on the structure of these materials: *PbS_61* and *PbS_23/CdS_15/ITO.* The irradiation process was also carried out in one of the EG-5 accelerator facility. In this case, the channel dedicated to ion implantation was used. In all cases, the material of the holders used was aluminium, although this was different for the sample irradiated with the first dose compared to that used to irradiate with the remaining doses. Fig. 6 shows the holders used for irradiation as well as an internal view of the irradiation chamber.
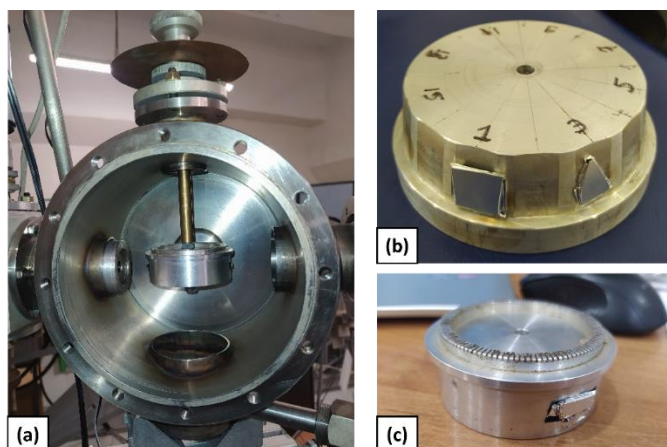
Figure 5: Some important parts of the experimental setup used for irradiation are shown: (a) irradiation chamber, (b) holder used for the sample at the first dose, and (c) holder used for the sample with the rest of the doses.

Before carrying out the irradiations, some aspects related to the effects of irradiation of these samples were simulated using SRIM-2008 software version 0.4. SRIM is a software package concerning the **S**topping and **R**ange of **I**ons in **M**atter. It has been continuously upgraded since its introduction in 1985 [20]. The physical foundations of this software are presented in detail in the book: *SRIM – The Stopping and Range of Ions in Matter* which can be accessed from reference [21]. Thanks to these simulations, the need to use an aluminium foil was detected to reduce the penetration

of ions into the sample reducing the damage, considering the small thickness of the PbS thin film samples.

From the experimental point of view, the registered doses appear tabulated below; besides, irradiation times varied from 1 min for the first dose to 2 hours of irradiation to reach the last dose.

Fluence $(protons/cm^2)$
$1.88 \cdot 10^{14}$
$1.13 \cdot 10^{15}$
$1.1 \cdot 10^{16}$
$1 \cdot 10^{17}$

The energy of the beam particles, ion flux density, and particle fluence necessary to achieve these dose values were also determined before proceeding to irradiate the samples. The mathematical expressions used appear below:

$$E = k \cdot q \cdot U$$

$$\phi = \frac{I}{S \cdot q}$$

$$D = \phi \cdot t$$

where k is a parameter that depends on the number of different charges present in the beam, q the charge of the electron, I the intensity of the beam (C/sec), S the surface area of the sample (cm^2) and t the irradiation time in seconds.

Discussion of the results obtained

RBS and PIXE processing results

The preliminary results of the processing of the RBS and PIXE spectra show that in the case of the *PbS_22/CdS_14/ITO* sample with the incidence of the ions in the normal direction to the sample surface, the ions only penetrated to the second layer, showing only three of the expected elements: lead, cadmium, and sulfur, as can be seen in Fig.6(a). The results show that at least in the first layers the total sulfur concentration represents double the sum of the concentrations of lead and cadmium respectively. Fig.6(b) shows the concentration profile detected in this case. The analysis of Fig.6(c), that correspond to the case of the study of this same sample but with the incidence of the ions forming an angle of 30° degrees with respect to the normal to the surface, the ions penetrate to the substrate, promoting the appearance of the contribution of the ITO substrate (oxygen, tin, and indium) in the RBS spectra, in addition to lead, sulfur and cadmium. From the point of view of the total

concentrations, it must be said that once again it is observed that the amount of sulfur exceeds the sum of the concentrations of cadmium and lead respectively at least from the second layer Fig.6(d). The above behavior is common in most of the samples studied, so a consultation with the group of researchers who participated in the growth of the samples becomes necessary to discuss the possible cause of this result.
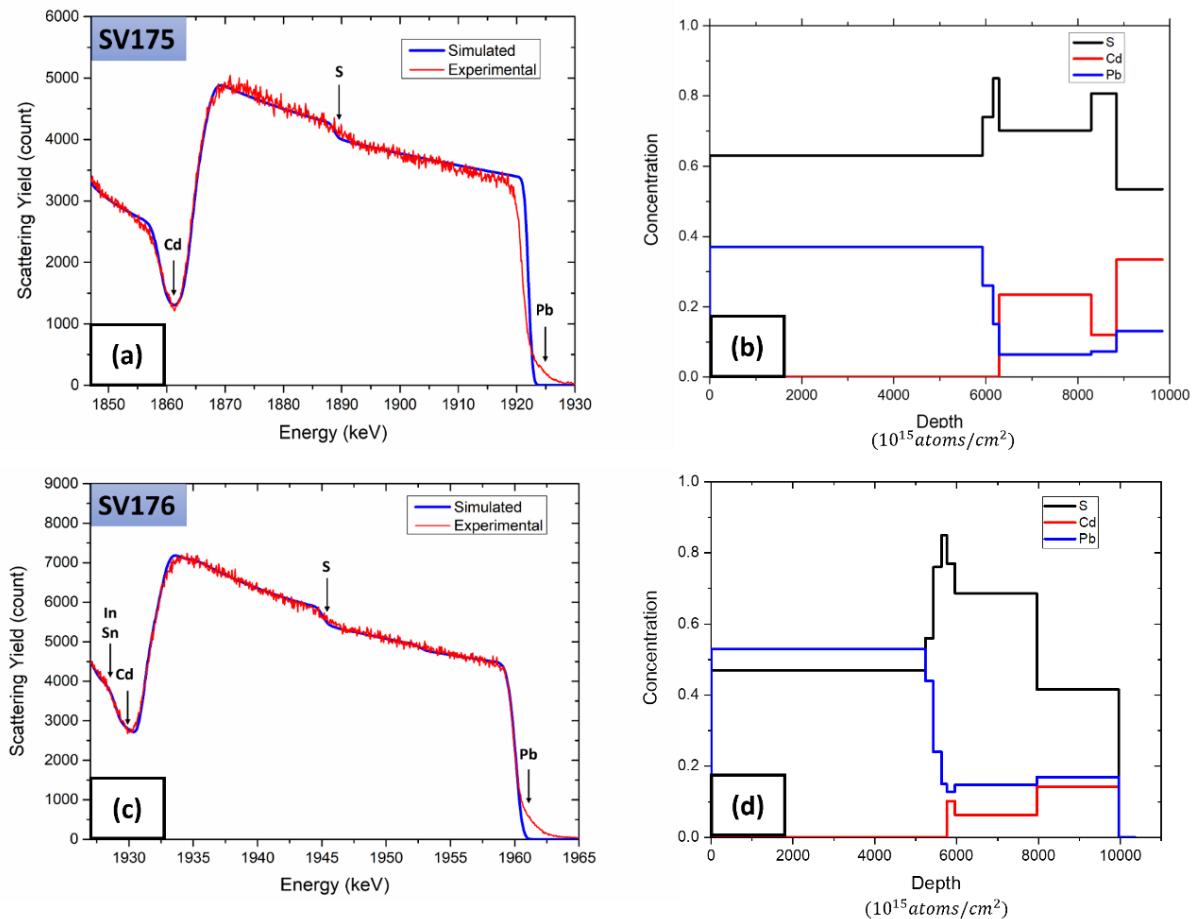
Figure 6: *RBS spectra (left column) and concentration profiles (right column). The upper part of the image shows the information corresponding to the results of the measurements with incidence of the ion beam in the direction normal to the surface of the PbS_22/CdS_14/ITO sample, while the lower part shows the information corresponding to the case of 30° incidence.*

The other interesting result of this part of the study corresponds to the detection in some cases of a certain traces of Argon in the surface of some samples, as can be seen in Fig.7(b)(d). Related to the above, it should be explained that initially as part of the PIXE processing a peak around 3.20keV was detected, as shown in Fig.8, which is very close to the tabulated X-ray emission energy corresponding to the K_α line of Ar (3.19keV). The possibility of possible contamination with Cadmium was also discussed since the L_α line of this element is around 3.13KeV, but this idea was discarded since the sample used corresponds to a single layer of PbS deposited on a BK7 substrate.

-Dubna, 2023-
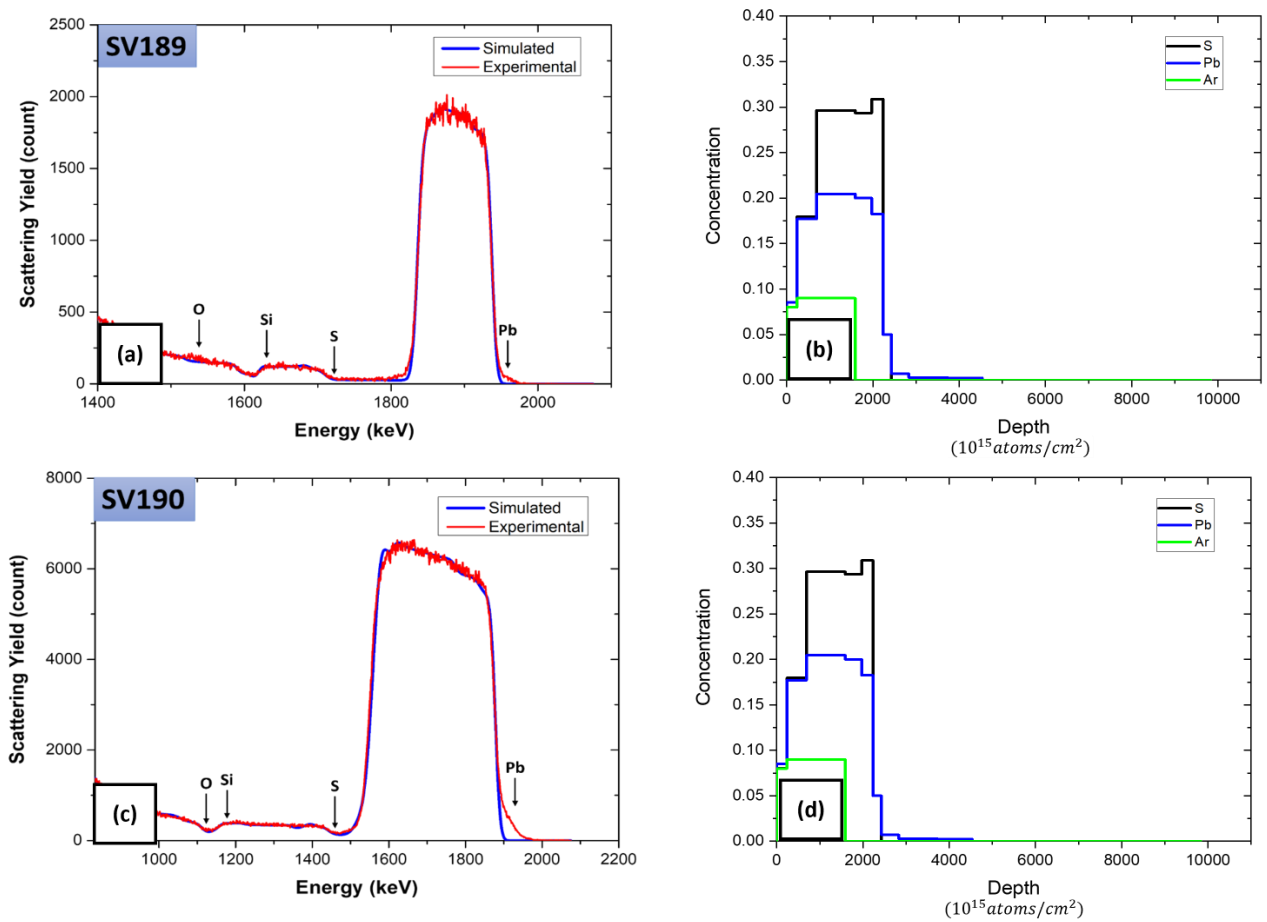
Figure 7: *RBS spectra (left column) and concentration profiles (right column). The upper part of the image shows the information corresponding to the results of the measurements with incidence of the ion beam in the direction normal to the surface of the Pb_47 sample, while the lower part shows the information corresponding to the case of 30° incidence.*
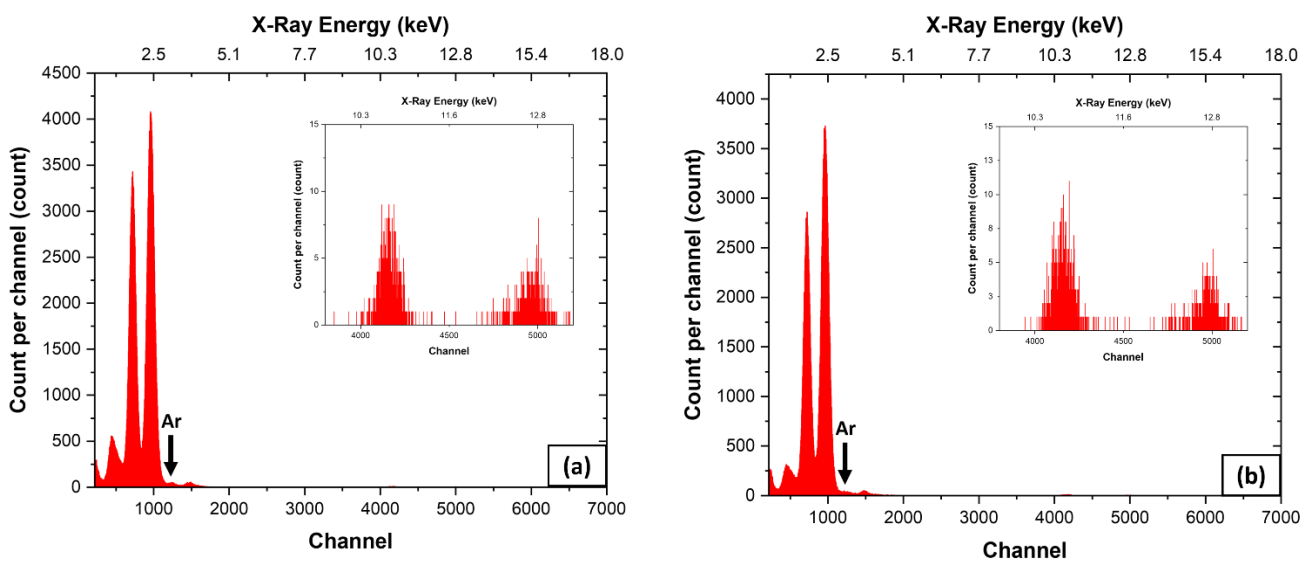
Figure 8: *PIXE spectrum corresponding to incidence angles of (a) 30° and (b) perpendicular incidence. In both spectra, the peaks corresponding to the contribution of Argon are noted.*

-Dubna, 2023-

This result was undoubtedly one of the most interesting because once it was discussed with the group of researchers who grew the samples, they showed great surprise at the non-reactivity of this element, even though it has been used as eroding gas.

Proton irradiation

As mentioned in the description of the materials and methods used for this research, once the values of all the experimental parameters necessary to obtain the desired doses were known, a simulation was carried out in the SRIM software before proceeding to the irradiation process. Related to the above, once the graphs of the number of events, vertical distribution, ionization, and energy range of the particles were obtained, the use of an aluminium foil (16 µm of thickness) was suggested due to the small thickness of the material of interest and to reduce both the penetration of protons and the great damage produced in the sample.

From the analysis of the simulation results in Fig.9 and Fig.10, we can deduce the high possibility of being successful in proton implantation using fundamentally a particle beam with an energy of approximately 1100keV.
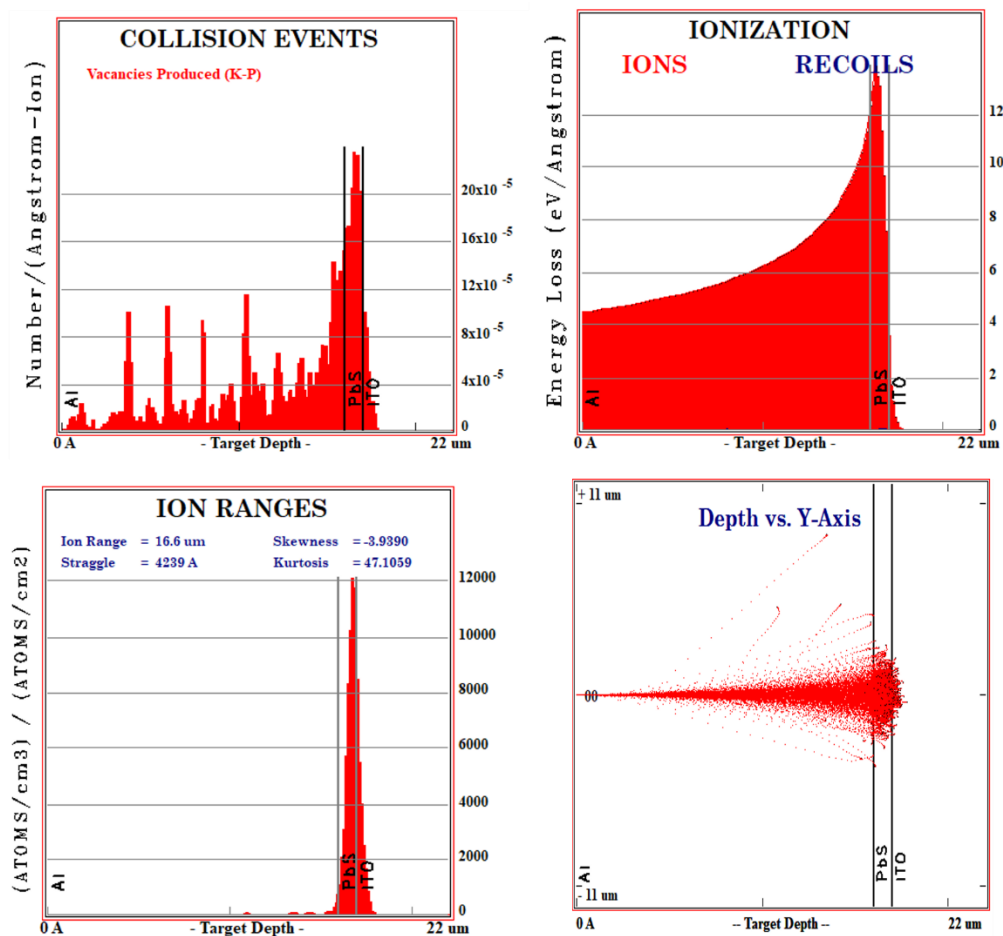
Figure 9: *Results of SRIM software simulations of the irradiation process for PbS_61 thin film sample for the first dose.*

-Dubna, 2023-
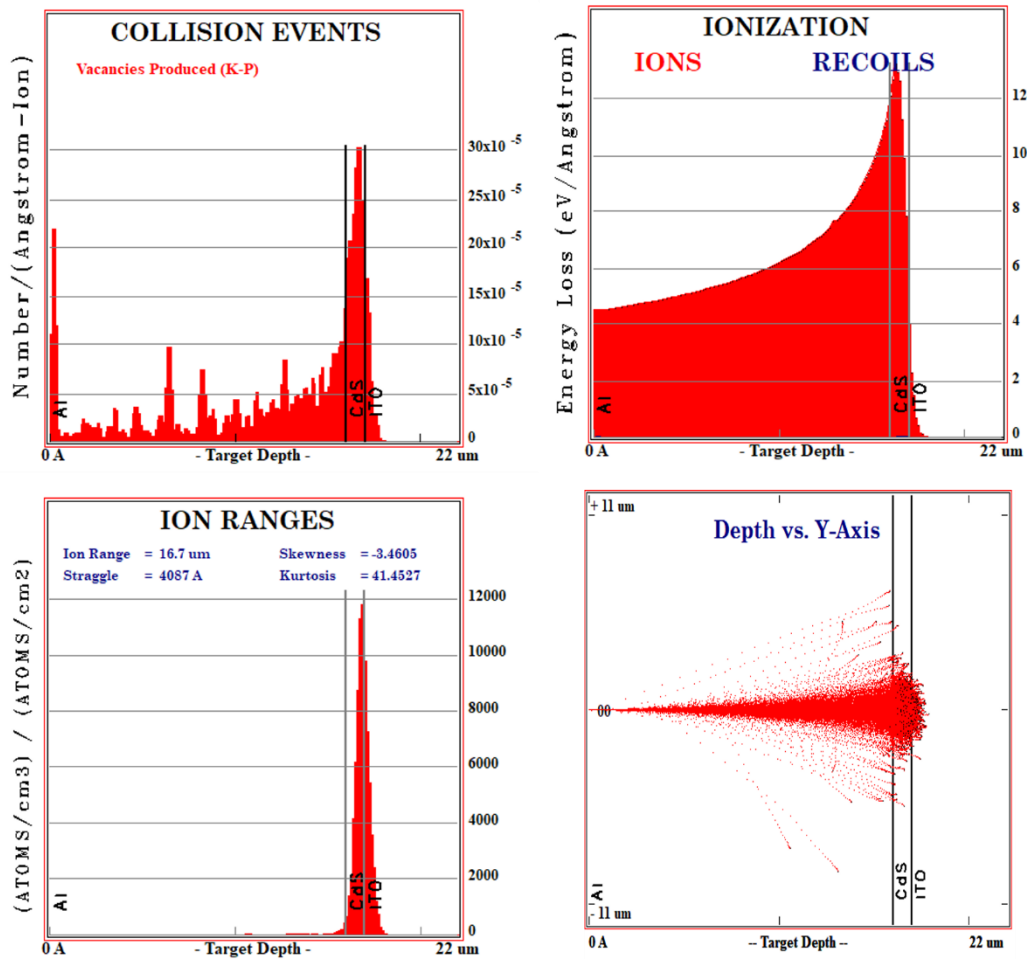
Figure 10: *Results of SRIM software simulations of the irradiation process for and PbS_23/CdS_15/ITO sample configuration for the first dose.*

Fig. 11 shows the images of both groups of samples after being irradiated with the different doses. The result of the preliminary analysis showed as the main result the possibility of identifying that the threshold dose that can cause significant macroscopic damage is within the range of $1.1 \cdot 10^{16}$ until $1 \cdot 10^{17} \ protons/cm^2$.
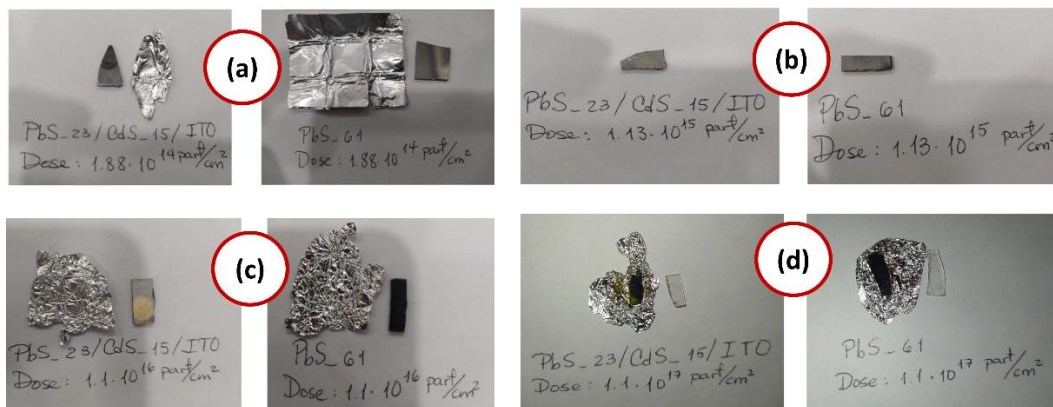
Figure 11: *Images of both types of samples taken after each irradiation process.*

-Dubna, 2023-

Conclusions

The preliminary results of these samples can be summarized as follows:

- It was obtained the profile of elemental concentrations of the PbS samples.

- The processing results of the RBS and PIXE spectra detected some Ar contamination in the sample labelled as *PbS_47* (150 W, 80 sccm, 30min).

- The presence of a certain degree of roughness in the external layers of the sample was confirmed.

- Most samples exhibit both the presence of a certain concentration gradient as well as an excess of sulfur.

- It was deduced that the threshold proton dose for which significant damage generated in both groups of materials is within the range: $1.1 \cdot 10^{16}$ - $1 \cdot 10^{17}$ $protons/cm^2$.

References

[1] Sadovnikov, S. I., Gusev, A. I., & Rempel, A. A. (2016). Nanostructured lead sulfide: synthesis, structure and properties. Russian Chemical Reviews, 85(7), 731–758. doi:10.1070/rcr4594

[2] Sadovnikov, S. I., Kozhevnikova, N. S., & Rempel, A. A. (2010). The structure and optical properties of nanocrytalline lead sulfide films. Semiconductors, 44, 1349-1356.

[3] Sadovnikov, S. I., Kozhevnikova, N. S., & Rempel, A. A. (2011). Stability and recrystallization of PbS nanoparticles. Inorganic Materials, 47, 837-843.

[4] Saikia, D., & Phukan, P. (2014). Fabrication and evaluation of CdS/PbS thin film solar cell by chemical bath deposition technique. Thin Solid Films, 562, 239-243.

[5] R.K. Joshi, A. Kanjilal, H.K. Sehgal, Appl. Surf. Sci. 221 (1–4) (2004) 43.

[6] N.I. Fainer, M.L. Kosinova, Yu.M. Rumyantsev, E.G. Salman, F.A. Kuznetsovh, Thin Solid Films 280 (1-2) (1996) 16.

[7] U. Madhu, N. Mukherjee, N.R. Bandyopadhyay, A. Mondal, Indian J. Pure Appl. Phys. 45 (2007) 226.

[8] A. Ashoour, Turk. J. Phys. 27 (2003) 551.

[9] Solis-Pomar, F., Cruz, A. F., Menchaca, J. L., Meléndrez, M. F., & Pérez-Tijerina, E. (2018). Study of the structural properties of nanostructured PbS thin films deposited by RF sputtering at room temperature. Materials Research Express, 5(10), 106403.

[10] Loferski, J. J. (1966). The effects of electron and proton irradiation on thin film solar cells. Revue de Physique Appliquee, 1(3), 221-227.

[11] J.L. Machol, F.W. Wise, R.C. Patel, D.B. Tanner, Phys. Rev. B 48 (4) (1993) 2819

[12] M.A. Halim, Nanomaterials 3 (2013) 22, http://dx.doi.org/10.3390/nano3010022.

[13] F.W. Wise, Acc. Chem. Res. 33 (11) (2000) 773.

[14] Nastasi, M., Mayer, J. W., & Wang, Y. (2014). *Ion beam analysis: fundamentals and applications*. CRC Press.

[15] M. Thompson, *RUMP: Rutherford backscattering spectroscopy analysis package*. http://www.genplot.com.

[16] E. Kótai, RBX: Simulation of RBS and ERD spectra. Can be obtained from the author.

[17] M. Mayer, *SIMNRA User's Guide*, Report IPP 9/113, Max-Planck-Institut für Plasmaphysik, Garching, Germany, 1997.

-Dubna, 2023-

[18] Johansson, S. A. (1989). PIXE: A novel technique for elemental analysis. Endeavour, 13(2), 48-53.

[19] Epp, J. (2016). X-ray diffraction (XRD) techniques for materials characterization. In Materials characterization using nondestructive evaluation (NDE) methods (pp. 81-124). Woodhead Publishing.

[20] J.F. Ziegler, J. Biersack, U. Littmark, ''The Stopping and Range of Ions in Matter", Pergamon Press, 1985

[21] J.F. Ziegler, J.P. Biersack, M.D. Ziegler, SRIM – The Stopping and Range of Ions in Matter", Ion Implantation Press, 2008. http://www.lulu.com/content/1524197.

<u>Acknowledgments</u>

-Dubna, 2023-

Anexo 1: RBS measurements experimental parameters

Sample Details	
Sample Label	PbS_22/CdS_14/ITO
Spectrum Label	SV175
Experimental Parameters	
Beam Intensity	2-2.2 µA
Incident Angle	0
Exit Angle	10
Scattering Angle	170
Energy per channel (keV/ch)	2.06
Flow (particles/sr)	$8·10^{10}$
Detector resolution (keV)	25
X_r^2 [channel range]	2.162 [200-850]

Sample Details	
Sample Label	PbS_22/CdS_14/ITO
Spectrum Label	SV176
Experimental Parameters	
Beam Intensity	2-2.2 µA
Incident Angle	30
Exit Angle	20
Scattering Angle	170
Energy per channel (keV/ch)	2.06
Flow (particles/sr)	$8·10^{10}$
Detector resolution (keV)	25
X_r^2 [channel range]	3.010 [200-850]

Sample Details	
Sample Label	PbS_41
Spectrum Label	SV177
Experimental Parameters	
Beam Intensity	2-2.2 µA
Incident Angle	30
Exit Angle	20
Scattering Angle	170
Energy per channel (keV/ch)	2.06
Flow (particles/sr)	$1.230·10^{11}$
Detector resolution (keV)	25
X_r^2 [channel range]	2.937 [150-900]

Sample Details	
Sample Label	PbS_41
Spectrum Label	SV178
Experimental Parameters	
Beam Intensity	2-2.2 µA
Incident Angle	0
Exit Angle	10
Scattering Angle	170
Energy per channel (keV/ch)	2.07
Flow (particles/sr)	$1.170 \cdot 10^{11}$
Detector resolution (keV)	25
X_r^2 [channel range]	2.432 [140-875]

Sample Details	
Sample Label	PbS_46
Spectrum Label	SV182
Experimental Parameters	
Beam Intensity	2 µA
Incident Angle	30
Exit Angle	20
Scattering Angle	170
Energy per channel (keV/ch)	2.07
Flow (particles/sr)	$3.08 \cdot 10^{10}$
Detector resolution (keV)	25
X_r^2 [channel range]	2.054 [150-900]

Sample Details	
Sample Label	PbS_46
Spectrum Label	SV183
Experimental Parameters	
Beam Intensity	2 µA
Incident Angle	0
Exit Angle	10
Scattering Angle	170
Energy per channel (keV/ch)	2.07
Flow (particles/sr)	$9.5 \cdot 10^{10}$
Detector resolution (keV)	25
X_r^2 [channel range]	2.185 [150-900]

Sample Details	
Sample Label	PbS_47
Spectrum Label	SV189
Experimental Parameters	
Beam Intensity	1.7-2 µA
Incident Angle	30
Exit Angle	20

Scattering Angle	170
Energy per channel (keV/ch)	2.07
Flow (particles/sr)	$5.5 \cdot 10^{10}$
Detector resolution (keV)	25
X_r^2 [channel range]	2.212 [150-850]

Sample Details	
Sample Label	PbS_47
Spectrum Label	SV190
Experimental Parameters	
Beam Intensity	1.7-2 µA
Incident Angle	0
Exit Angle	10
Scattering Angle	170
Energy per channel (keV/ch)	2.07
Flow (particles/sr)	$1.9 \cdot 10^{11}$
Detector resolution (keV)	25
X_r^2 [channel range]	2.546 [150-875]

-Dubna, 2023-

Anexo 2: Energy calibration parameters and verification of RBS spectra.
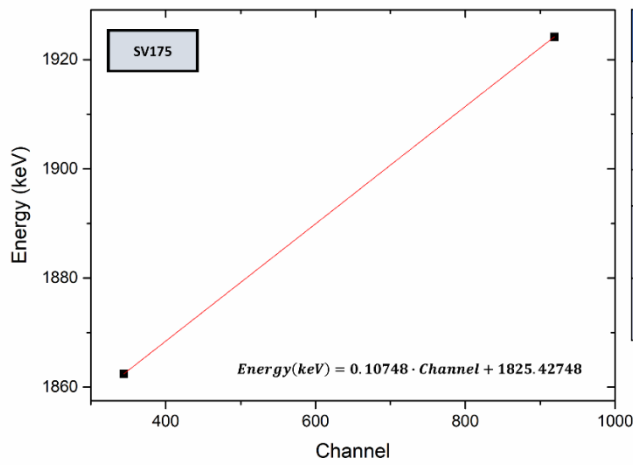
Calibration parameters		
Elemental Peaks	**Channels**	**Expected Energy (keV)**
Pb	919	1924.2
Cd	344	1862.4
Verification		
S	616	1556 (Theoretical)
		1891.63516 (Experimental)
Fitting Uncertainty	± 335.64 keV	

$$Energy(keV) = 0.10748 \cdot Channel + 1825.42748$$
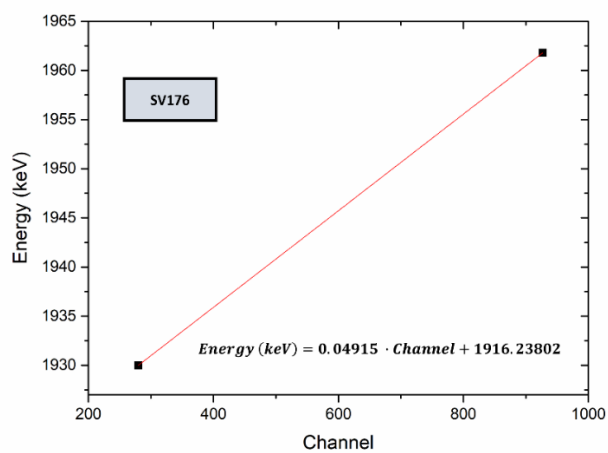
Calibration parameters		
Elemental Peaks	**Channels**	**Expected Energy (keV)**
Pb	927	1961.8
Cd	280	1930
Verification		
S	615	1764.6 (Theoretical)
		1946.46527 (Experimental)
Fitting Uncertainty	± 181.86527 keV	

$$Energy\,(keV) = 0.04915 \cdot Channel + 1916.23802$$
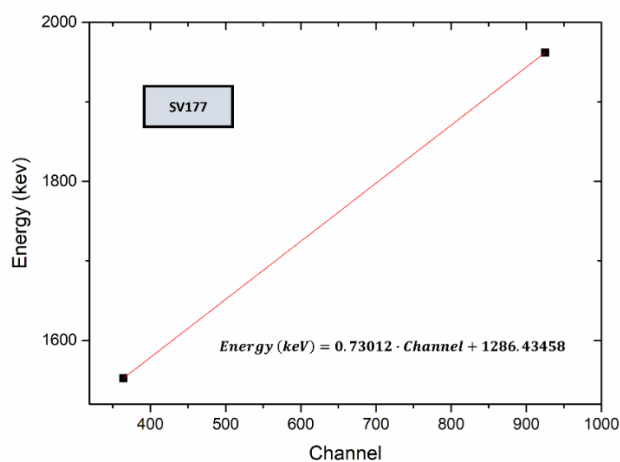
Calibration parameters		
Elemental Peaks	**Channels**	**Expected Energy (keV)**
Pb	925	1961.8
Cd	364	1930
Verification		
S	614	1764.6 (Theoretical)
		1734.72826 (Experimental)
Fitting Uncertainty	±29.87174 keV	

$$Energy\,(keV) = 0.73012 \cdot Channel + 1286.43458$$

-Dubna, 2023-
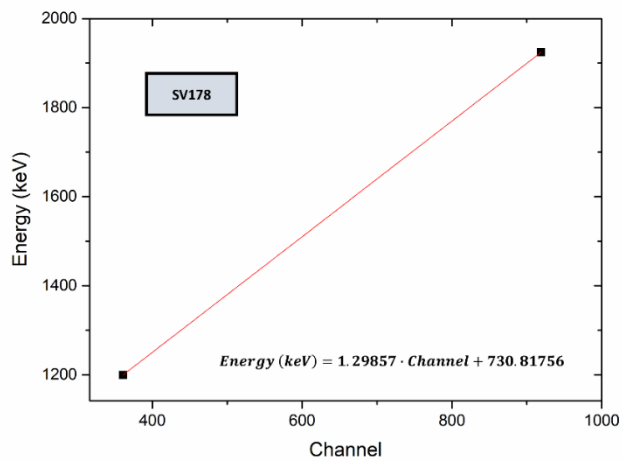
Calibration parameters		
Elemental Peaks	**Channels**	**Expected Energy (keV)**
Pb	919	1924.2
O	361	1924.2
Verification		
S	609	1556 (Theoretical)
		1521.64669 (Experimental)
Fitting Uncertainty	±34.35331 keV	

$$Energy\ (keV) = 1.29857 \cdot Channel + 730.81756$$
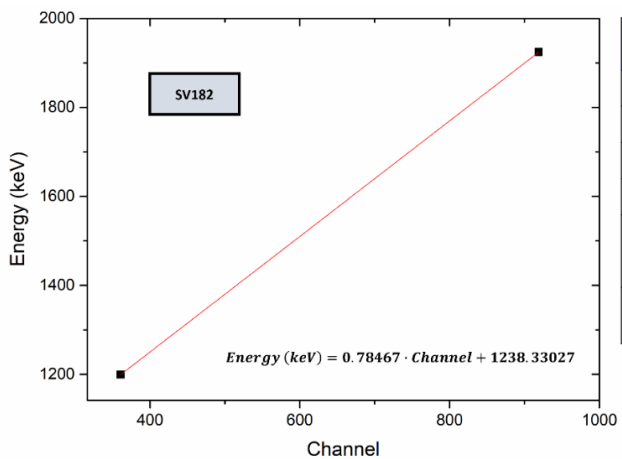
Calibration parameters		
Elemental Peaks	**Channels**	**Expected Energy (keV)**
Pb	922	1961.8
O	400	1552.2
Verification		
Si	540	1733.2 (Theoretical)
		1662.05207 (Experimental)
Fitting Uncertainty	± 71.14793 keV	

$$Energy\ (keV) = 0.78467 \cdot Channel + 1238.33027$$
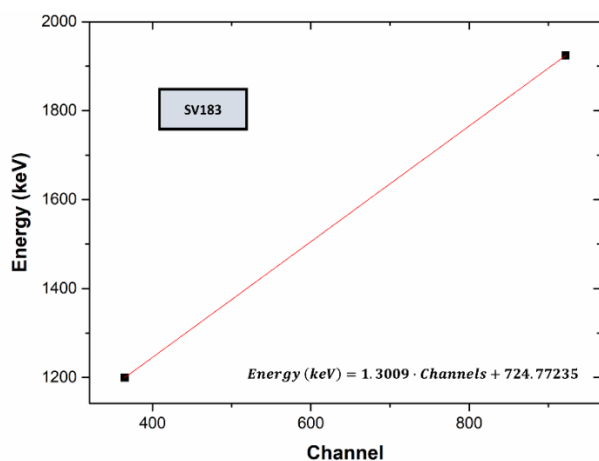
Calibration parameters		
Elemental Peaks	**Channels**	**Expected Energy (keV)**
Pb	922	1924.2
O	365	1199.6
Verification		
Si	454	1501 (Theoretical)
		1315.38095 (Experimental)
Fitting Uncertainty	± 185.61905 keV	

$$Energy\ (keV) = 1.3009 \cdot Channels + 724.77235$$

-Dubna, 2023-
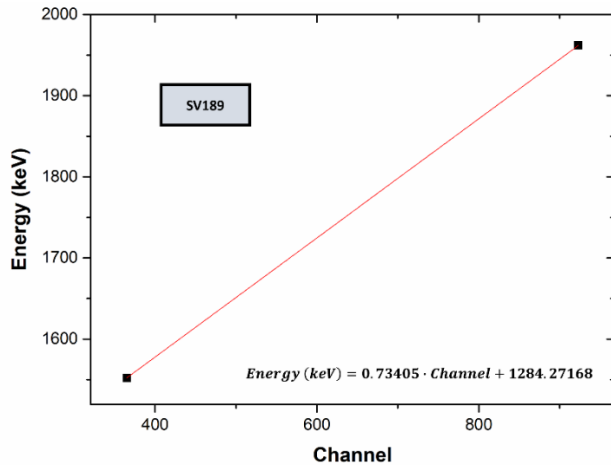
Calibration parameters

Elemental Peaks	Channels	Expected Energy (keV)
Pb	923	1961.8
O	365	1552.2
Verification		
S	614	1764.6 (Theoretical)
		1734.97838 (Experimental)
Fitting Uncertainty	± 29.62162 keV	

$$Energy\ (keV) = 0.73405 \cdot Channel + 1284.27168$$

SV189
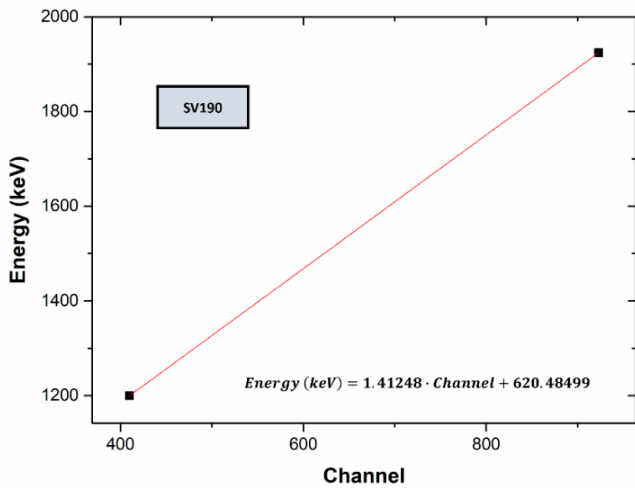
Calibration parameters

Elemental Peaks	Channels	Expected Energy (keV)
Pb	923	1924.2
O	410	1199.6
Verification		
S	610	1556 (Theoretical)
		(Experimental)
Fitting Uncertainty	± keV	

$$Energy\ (keV) = 1.41248 \cdot Channel + 620.48499$$

SV190

-Dubna, 2023-